

Efficient and robust numerical treatment of a gradient-enhanced damage model at large deformations

Philipp Junker¹  | Johannes Riesselmann²  | Daniel Balzani² 

¹Institute of Continuum Mechanics, Leibniz University Hannover, Hannover, Germany

²Chair of Continuum Mechanics, Ruhr University Bochum, Bochum, Germany

Correspondence

Philipp Junker, Institute of Continuum Mechanics, Leibniz University Hannover, Hannover, Germany.

Email: philipp.junker@rub.de

Abstract

The modeling of damage processes in materials constitutes an ill-posed mathematical problem which manifests in mesh-dependent finite element results. The loss of ellipticity of the discrete system of equations is counteracted by regularization schemes of which the gradient enhancement of the strain energy density is often used. In this contribution, we present an extension of the efficient numerical treatment, which has been proposed by Junker et al. in 2019, to materials that are subjected to large deformations. Along with the model derivation, we present a technique for element erosion in the case of severely damaged materials. Efficiency and robustness of our approach is demonstrated by two numerical examples including snapback and springback phenomena.

KEYWORDS

element erosion technique, finite difference methods, finite element methods, gradient-enhanced damage, snapback, springback

1 | INTRODUCTION

The modeling of damage at finite strains roots back to the eighties of the 20th century when first phenomenological models related to material degradation were developed. These models were mainly constructed based on the original ideas for small strains where damage was considered as a reduction of the effective cross section area on which the load acts resulting from the nucleation and evolution of cavities. The reduced cross section thus softens the material which gives rise to the stress- and strain-softening effects. On a material point level, this means that the stress reduces with increasing strains after a critical threshold value is reached. This phenomenological approach of describing the complex microstructural processes during material failure, that might be accompanied by the evolution of dislocations, micro-cracks and delamination effects, provides a convincing method for material modeling. Unfortunately, softening may also be accompanied by a loss of ellipticity of the system of governing equations once a certain amount of damage has evolved which renders boundary value problems ill-posed. An obvious indicator for such problems are severe dependencies of the finite element results on the individual mesh discretization: the smaller the finite element size is chosen, the more localized resulting damage bands will be. Furthermore, and even worse, the numerical solution of such problems does not converge and might be unstable regarding small perturbations of the boundary conditions, that is, they lack numerical robustness. These effects are not only observed at the level of spatial distribution of the damage variable but also for the global behavior in terms of reaction forces.^{1,2} Consequently, a mathematical correction of the problem is inevitable. This process is referred to as regularization which might be performed in time and space. Overview articles may be found, for example, in References 3 and 4.

This is an open access article under the terms of the Creative Commons Attribution-NonCommercial License, which permits use, distribution and reproduction in any medium, provided the original work is properly cited and is not used for commercial purposes.

© 2021 The Authors. *International Journal for Numerical Methods in Engineering* published by John Wiley & Sons Ltd.

Alternatively, a relaxed variational formulation might be employed which relies on a careful analysis of the convexity properties of the underlying energy. This energetic analysis demands a direct formulation of the damage variable as pure function of the deformation state such that the condensed energy (energy plus time-integrated dissipation) may be relaxed. It is thus convenient to formulate the model in a time-incremental way, compare References 5-8. Thereby, a dissipative material behavior may be described by an incrementally hyperelastic representation, which is thus open for analysis with respect to generalized convexity conditions. This enables the construction of convex hulls (see Reference 9 for small strains and References 10 and 11 for finite strains) which on the one hand ensures the recovery of ellipticity and on the other hand guarantees the existence of minimizers. In contrast to spacial regularization approaches, no internal length scale parameter has to be chosen since the micromechanical parameters are obtained as result of the convexification procedure. On the other hand, the effort at the material point level may be increased if a nonconvex minimization problem is solved as part of the convexification at each integration point, which yields an increased expense in the assembling procedure. Another drawback may be seen in the fact that although the stress softening hysteresis as explained above may in principle be captured, a softening in the sense of negative tangents in stress-strain curves can not yet be modeled at the material point. One exception so far is the approach of Schwarz et al. in Reference 12 for small strains, where a simplified microstructure consisting of damaged, linear elastic materials and whose resulting convexified energy indeed enables the description of strain-softening.

In the context of time-wise regularization, viscous effects are included into the model. Examples for such models may be found in References 3,13-17. These models introduce a rate-dependence of the damage evolution which damps the local reduction of stiffness. Consequently, damage evolves also at neighbored material points to keep the amount of dissipated energy constant. A huge benefit of such models (as well as of relaxed incremental formulations) is their implementability in any finite element framework using solely the material law interface. However, viscous damage models possess a remarkable drawback: the viscosity associated to damage evolution has to be chosen quite high, reaching values that are unphysical in order to obtain the desired regularization. Furthermore, the effectiveness of viscous regularization strongly depends on the applied loading velocity which does not necessarily need to agree with experimental velocities. Finally, the interplay of viscosity and loading velocity has to be set and thus well-posedness has to be proven for each individual boundary value problem rendering such approaches rather impractical for application.

Spacial regularization “homogenizes” the damage evolution on a local level. To this end, either integral formulations are introduced or a gradient enhancement of the strain energy is employed. A major benefit of such models as compared to viscous regularization is that it can be shown that they are inherently well-posed. Examples for spatially regularized damage models may be found, for example, in References 1,2,18-23. Also for the finite-strain regime, they have been used, compare References 24-31. Such models may be applied to arbitrary loading velocities since any dependence of the material behavior on this boundary condition is included in a physically sound manner. Furthermore, they might be coupled to other physical processes as for instance plasticity and temperature dependence without unphysical parameters being present in the complete system of model equations. For gradient regularization, we refer to the prototype approach of References 19,20 and similarly Reference 21, and its finite-strain extension in Reference 30, where a nonlocal function carries information on the damage state. This procedure transforms the associated equation for the damage state from a local evolution equation at the material point (as is the case for viscous regularization) to a field equation (integral equation for integral regularization or partial differential equation for gradient regularization) which has to be solved along with the balance of linear momentum for the displacements. Consequently, the number of unknowns increases during numerical treatment, for example, the number of nodal variables increases from three (displacements) to four (displacements + damage state variable) in a mixed finite element implementation. While thermodynamic consistency and mesh-independent simulations can be ensured with these approaches, unfortunately, the increased number of degrees of freedom in the discrete global system of equations significantly increases computational costs.

To limit the usual numerical deficiency of gradient regularization, we present in this contribution a novel finite strain gradient damage formulation. A similar approach for the small strain regime has been introduced in Reference 32 (see also Reference 33 for a detailed numerical analysis including mesh adaptivity). The model for the small strain regime has proven to consume a limited amount of extra computation effort than purely elastic simulations which constitute the reference for the shortest simulation time. Furthermore, the model has proven to be numerically robust, compare Reference 33. Both aspects, computation speed and numerical robustness, are investigated for the novel gradient-enhanced damage model when formulated and evaluated for the finite strain regime in this contribution. To this end, we begin with the variational derivation of the damage model that is formulated in terms of a partial differential inequality which complements the partial differential equation describing the balance of linear momentum. Then, we apply the neighbored

element method which has proven to be beneficial for a robust and time-efficient numerical evaluation of the set of governing equations given by the balance of linear momentum and an additional field equation. Examples have been given in the context of small-strain damage^{32,33} and small-strain³⁴ and finite-strain topology optimization.³⁵ The neighbored element method combines a finite element approach for the balance of linear momentum and a finite difference approach for the additional field equation along with operator splitting techniques. Thereby, the neighbored element method conserves the size of the global system of equations resulting from the finite element formulation for the displacements: to be more precise, the number of nodal unknowns for the finite elements remains unchanged from a corresponding purely elastic formulation. The partial differential inequality for the damage state, however, is solved through a correspondingly modified internal update procedure. Furthermore, a novel stabilization technique based on element erosion methods enables us to obtain numerical results even for substantial deformation states including regions of highly damaged material for which the model is close to the loss of its validity. The numerical results show mesh-independence while requiring minimal extra computation time compared to purely hyperelastic simulations.

2 | A GRADIENT-ENHANCED DAMAGE MODEL AT FINITE STRAINS

There exist various strategies for the derivation of fundamental material models of which an extended Hamilton principle offers a variational approach. Its stationarity conditions agree with the second Law of Thermodynamics and Onsager's principle by construction if physically reasonable ansatzes for the strain energy density and the dissipation function are chosen. For details on the extended Hamilton principle and its relation to thermodynamics and other modeling strategies, such as the principle of virtual work or the principle of the minimum of the dissipation potential, we refer to Reference 36.

The extended Hamilton principle is related to the stationarity of the action function. It can be shown, compare Reference 36, that it constitutes as the following condition: for the quasi-static case, the sum of the Gibbs energy \mathcal{G} , which is also referred to as total potential, and the work due to dissipative processes \mathcal{D} tends to be stationary:

$$\mathcal{H}[\mathbf{u}, \alpha] := \mathcal{G}[\mathbf{u}, \alpha] + \mathcal{D}[\alpha] \rightarrow \underset{\mathbf{u}, \alpha}{\text{stat.}} \quad (1)$$

A detailed investigation of the extended Hamilton principle as unifying theory for coupled problems, that is, thermo-mechanical processes, and dissipative microstructure evolution has been presented in Reference 36.

In (1), the displacements are denoted by \mathbf{u} and the state of microstructure is expressed in terms of the internal variable α . The Gibbs energy reads

$$\mathcal{G}[\mathbf{u}, \alpha] = \int_{\Omega} \Psi(\mathbf{C}, \alpha) \, dV - \int_{\Omega} \mathbf{b}^* \cdot \mathbf{u} \, dV - \int_{\partial\Omega} \mathbf{t}^* \cdot \mathbf{u} \, dA \quad (2)$$

with the strain energy density Ψ , the prescribed body forces \mathbf{b}^* , and the traction vector \mathbf{t}^* . The integrals are evaluated for the body's volume Ω and its surface $\partial\Omega$ in its reference configuration with the position vector \mathbf{X} . The deformation is measured by the right Cauchy Green tensor $\mathbf{C} := \mathbf{F}^T \mathbf{F}$ with the deformation gradient $\mathbf{F} = \partial \mathbf{x} / \partial \mathbf{X} = \mathbf{I} + \mathbf{u} \otimes \nabla$ and the spatial coordinate $\mathbf{x} = \mathbf{X} + \mathbf{u}$ in the current configuration. Throughout this contribution, the nabla operator is computed with respect to the reference configuration, that is, $\nabla \equiv \nabla_{\mathbf{X}}$.

The work due to dissipative processes is given by

$$\mathcal{D}[\alpha] := \int_{\Omega} p^{\text{diss}} \alpha \, dV \quad (3)$$

when the non-conservative force p^{diss} performs work "along" the microstructure state which is described in terms of the internal variable α . The stationarity condition of (1) thus reads

$$\delta \mathcal{H}[\mathbf{u}, \alpha](\delta \mathbf{u}, \delta \alpha) = \delta \mathcal{G}[\mathbf{u}, \alpha](\delta \mathbf{u}, \delta \alpha) + \delta \mathcal{D}[\alpha](\delta \alpha) = 0 \quad \forall \delta \mathbf{u}, \delta \alpha \quad (4)$$

with

$$\delta \mathcal{G}[\mathbf{u}, \alpha](\delta \mathbf{u}, \delta \alpha) = \int_{\Omega} (\delta_{\mathbf{u}} \Psi(\mathbf{C}, \alpha) \, dV + \delta_{\alpha} \Psi(\mathbf{C}, \alpha)) \, dV - \int_{\Omega} \mathbf{b}^* \cdot \delta \mathbf{u} \, dV - \int_{\partial\Omega} \mathbf{t}^* \cdot \delta \mathbf{u} \, dA. \quad (5)$$

The non-conservative force is assumed to be a material-specific quantity which is determined once the process conditions are set, similarly as the external forces \mathbf{b}^* and \mathbf{t}^* . Consequently, it does not follow from a stationarity condition but it needs to be modeled. This implies $\delta_\alpha p^{\text{diss}} = 0$ such that the variation of the dissipated energy reads

$$\delta D[\alpha](\delta\alpha) = \int_{\Omega} p^{\text{diss}} \delta\alpha \, dV. \tag{6}$$

Since the variations for displacements and microstructural state are independent, we obtain

$$\begin{cases} \int_{\Omega} \delta\mathbf{u} \Psi(\mathbf{C}, \alpha) \, dV - \int_{\Omega} \mathbf{b}^* \cdot \delta\mathbf{u} \, dV - \int_{\partial\Omega} \mathbf{t}^* \cdot \delta\mathbf{u} \, dA = 0 & \forall \delta\mathbf{u} \\ \int_{\Omega} \delta_\alpha \Psi(\mathbf{C}, \alpha) \, dV + \int_{\Omega} p^{\text{diss}} \delta\alpha \, dV = 0 & \forall \delta\alpha \end{cases}. \tag{7}$$

Specifications of the strain energy density Ψ and the non-conservative force p^{diss} allow the application of the latter equations for the derivation of models for various materials. The condition (7)₂ is valid both for rate-independent and rate-dependent processes. For the rate-independent case, this condition immediately defines the evolution equation for the internal variable α . However, the necessary damage criterion is received later by performing a Legendre transformation of the dissipation function which defines the non-conservative force p^{diss} . More details are presented later.

Based thereon, let us provide specific formulas for a gradient-enhanced damage model by first setting the internal variable α as damage variable. Then, we define the strain energy density by

$$\Psi(\mathbf{C}, \alpha) = (1 - D(\alpha)) \Psi_0(\mathbf{C}) + \frac{1}{2} \beta ||\nabla f||^2 \tag{8}$$

with the damage function $D(\alpha) := 1 - f(\alpha)$ and $f(\alpha) = \exp(-\alpha)$. The damage function needs to be bounded such that $D \in [0, 1]$ where $D = 0$ refers to the undamaged and $D = 1$ to the fully damaged state. The relations for f are thus, $f = 1$ for the intact material and $f = 0$ for the failed material. We consequently demand $f \in [0, 1]$ which is ensured for our choice $f = \exp(-\alpha)$ when $\alpha \in [0, \infty[$. Then, the undamaged state can be indicated by $\alpha = 0$ and the fully damaged state by $\alpha \rightarrow \infty$. Concluding, the damage state can be equivalently be expressed in terms of D, f , and α . The motivation for the introduction of these quantities is that the relation $1 - D(\alpha)$ corresponds to the primal idea of modeling damage by relating the intact and failed cross section areas to each other, compare References 37,38. Then, the damage function $D(\alpha)$ must be a monotonically increasing function in the damage variable α . An suitable representation is provided by $D(\alpha) = 1 - f(\alpha)$ when f is monotonically decreasing. Here, different approaches are possible, for example, polynomials, see Reference 16. However, for our model, the exponential choice, which was proposed in Reference 21, is more convenient due to the property $f' = -f$ as will be seen later.

The parameter β serves as regularization parameter and thus controls the thickness of the damage zone. The formulation of the strain energy density is the same approach as in Reference 32; however, in contrast to the original work which was restricted to small deformations, we now make use of a hyperelastic strain energy density of the undamaged material $\Psi_0 = \Psi_0(\mathbf{C})$.

The non-conservative force is usually derived from a dissipation function Δ^{diss} such that

$$p^{\text{diss}} = \frac{\partial \Delta^{\text{diss}}}{\partial \dot{\alpha}} \tag{9}$$

holds. Therefore, it is rather the dissipation function Δ^{diss} which needs to be modeled instead of the non-conservative force p^{diss} . This agrees to other modeling principles, for example, the principle of maximum dissipation for elasto-plasticity, in which the yield function is modeled directly. The associated dissipation function could then be obtained by Legendre transforming the yield function. For more details on the relation of these modeling principles and their thermodynamic relation, we refer, for example, to References 36,39,40. For rate-independent microstructural evolution, which is the case for the present model for damage evolution, functions have to be used that are homogeneous of order one. Hence, the dissipation function

$$\Delta^{\text{diss}} := r|\dot{\alpha}| \tag{10}$$

is used³² from which

$$p^{\text{diss}} = \partial\Delta^{\text{diss}} := \begin{cases} r \frac{\dot{\alpha}}{|\dot{\alpha}|} & \text{for } \dot{\alpha} \neq 0 \\ \{-r, r\} & \text{for } \dot{\alpha} = 0 \end{cases} \quad (11)$$

follows. The parameter r is referred to as dissipation parameter and it will become obvious that it represents an energetic threshold value for the onset and evolution of damage. It is worth mentioning that the partial derivative in (9) transforms to a subdifferential in our case since $\partial\Delta^{\text{diss}}/\partial\dot{\alpha}$ is not unique at $\dot{\alpha} = 0$ for our rate-independent ansatz for Δ^{diss} in (10). Then, the stationarity condition (7)₁ result in the weak form of the balance of linear momentum

$$\int_{\Omega} \mathbf{S} : \frac{1}{2} \delta \mathbf{C} \, dV - \int_{\Omega} \mathbf{b}^* \cdot \delta \mathbf{u} \, dV - \int_{\partial\Omega} \mathbf{t}^* \cdot \delta \mathbf{u} \, dA = 0 \quad \forall \delta \mathbf{u}, \quad (12)$$

where $\mathbf{S} = 2\partial\Psi(\mathbf{C}, \alpha)/\partial\mathbf{C}$ denotes the Second Piola Kirchhoff stress tensor. The stationarity condition in (7)₂ reads

$$\int_{\Omega} f' \Psi_0 \delta \alpha \, dV + \int_{\Omega} \beta \nabla f \cdot \nabla (f' \delta \alpha) \, dV + \int_{\Omega} \partial\Delta^{\text{diss}} \delta \alpha \, dV = 0 \quad (13)$$

where we considered $\delta_{\alpha} f = f' \delta \alpha$. Integration by parts of the second term results in

$$\int_{\Omega} \beta f' \nabla f \cdot \nabla \delta \alpha \, dV = \int_{\partial\Omega} \beta f' \mathbf{n}_0 \cdot \nabla f \delta \alpha \, dA - \int_{\Omega} \beta f' \Delta f \delta \alpha \, dV \quad (14)$$

and thus, (13) transforms to

$$- \int_{\Omega} (f \Psi_0 - \beta f \Delta f - \partial\Delta^{\text{diss}}) \delta \alpha \, dV - \int_{\partial\Omega} \beta f \mathbf{n}_0 \cdot \nabla f \delta \alpha \, dA = 0 \quad (15)$$

due to $f' = -f$. The local evaluation of the first integral in (15) results in the differential inclusion

$$f \Psi_0 - \beta f \Delta f - \partial\Delta^{\text{diss}} \ni 0 \quad \forall \mathbf{X} \in \Omega \quad (16)$$

due to the set-valued character of the subdifferential $\partial\Delta^{\text{diss}}$. Therefore, it is convenient to perform a Legendre transformation such that we transform the dissipation function, which is formulated in terms of the thermodynamic flux $\dot{\alpha}$, into a function $\tilde{\Delta}^{\text{diss}}$ which depends on the thermodynamic force $p := f \Psi_0 - \beta f \Delta f$. Consequently, we obtain

$$\tilde{\Delta}^{\text{diss}} = \sup_{\dot{\alpha}} \{p \dot{\alpha} - \Delta^{\text{diss}}\} = \sup_{\dot{\alpha}} \{|\dot{\alpha}|(p \operatorname{sgn} \dot{\alpha} - r)\}. \quad (17)$$

Healing in the sense of an increasing stiffness contradicts our motivation to model damage. Thus, the sign of the rate of the damage variable is $\operatorname{sgn} \dot{\alpha} = \{0, 1\}$ and the Legendre transform reads

$$\tilde{\Delta}^{\text{diss}} = \begin{cases} 0 & \text{if } p - r \leq 0 \\ \infty & \text{else} \end{cases} \quad (18)$$

which is the indicator function associated to the current damage model. From the first case, we identify

$$\begin{cases} p < r : & \dot{\alpha} = 0 \\ p = r : & \dot{\alpha} > 0 \end{cases} \quad (19)$$

It is thus convenient to introduce the function $\Phi := p - r$ which separates stationarity of the damage state for $\Phi < 0$ and evolution of the damage state for $\Phi = 0$. The function fulfills a similar purpose as yield functions in models for elasto-plasticity. The parameter r has a similar meaning as a scalar-valued yield stress. However, it is an energetic threshold value for the present case of damage. In case a weakened softening behavior shall be considered, the model can be

easily adapted by choosing a non-constant dissipation parameter $r = r(\alpha)$ which is a monotonically increasing function in α . This adaption of the model results in a behavior which can be compared to hardening in plasticity. Consequently, the evolution of damage is slowed down. The entire model derivation remains unmodified. In the current work, however, we concentrate on the perfectly brittle damage behavior with maximum damage evolution and a sudden failure of the component. This is associated by a vertical branch in the force/displacement curve. This behavior indicates that the non-coercivity of the related condensed energy $\Psi^c := (1 - D(\alpha))\Psi_0(\mathbf{C}) + \int \Delta^{\text{diss}} dt$ has maximum intensity for the brittle case such that it constitutes the most complex behavior from a numerical perspective. Furthermore, the model accounts only for two stages of material behavior, that is, for the elastic case and the case of damage evolution. To be more precise, the applicability of the model to practical applications can be significantly increased by including also the evolution of plastic deformations. Examples on the modeling of plasticity by using Hamilton's principle or related variational principles are given, for example, in References 36,41. In addition to that, structural boundary value problems may occur where large deformations appear while the strains stay only moderate. Then, even materials not behaving plastically may be considered in structural problems where large deformations occur. This is why we included the u-shaped specimen in the numerical results, see Figure 8. In these cases of large deformations, it becomes obvious that equilibrium of forces has to be computed in the current configuration. This is a priori included in the geometrically nonlinear setting of finite deformations. Note that although classical engineering materials allowing for large strains usually include plastic deformations, there exist materials such as soft biological tissues where the plastic deformations are small although large strains and a softening response appear. Concluding, we limit ourselves to the case without plasticity for the current presentation and postpone it to future investigations.

Finally, we can collect the governing equations for damage evolution in the following form

$$\dot{\alpha} \geq 0, \quad \Phi := f\Psi_0 - \beta f \Delta f - r \leq 0, \quad \Phi \dot{\alpha} = 0 \quad \forall \mathbf{X} \in \Omega \tag{20}$$

which are identified as Karush Kuhn Tucker conditions. It is worth mentioning that we obtain a similar equation as other works with gradient enhancement of the free energy density (e.g., References 19,21. However, in contrast to other works, the Laplace term in the governing Equation (20) is scaled by f . Consequently, the impact of the Laplace term is continuously reduced as damages evolves and consequently $f \rightarrow 0$. Therefrom, it can be concluded that the partial differential inequality reduces to $-r \leq 0$ for complete damage, that is, when $f = 0$; it is thus identically fulfilled. This property is not ensured a priori when the usual gradient of the damage variable is considered such that an inequality of the form $f\Psi_0 - \beta \Delta \alpha - r \leq 0$ needs to be fulfilled. This inequality reduces to $-\beta \Delta \alpha - r \leq 0$ for $f \rightarrow 0$ which might not possess a (local) solution when $\Delta \alpha < 0$. However, a rigorous mathematical analysis of the natural modification of the Laplace term when the gradient of f is used instead of the gradient of α , unfortunately, cannot be given in this contribution, but remains an open problem. As will be shown by the numerical results, we observe a smooth and fast convergence of the model both for mesh and time discretization, compare Section 4.

The surface integral in (15) constitutes as Neumann condition

$$\mathbf{n}_0 \cdot \nabla f = 0 \quad \forall \mathbf{X} \in \partial\Omega \tag{21}$$

for f . Here, \mathbf{n}_0 denotes the normal vector on the surface $\partial\Omega$ in the reference configuration. More details on the fundamentals of the damage model can be found in the original publication.³²

3 | NUMERICAL TREATMENT

The model above consists of two unknowns: the displacement field \mathbf{u} and the damage variable α . They can be determined by solving

$$\begin{cases} \int_{\Omega} \mathbf{S} : \frac{1}{2} \delta \mathbf{C} dV - \int_{\Omega} \mathbf{b}^* \cdot \delta \mathbf{u} dV - \int_{\partial\Omega} \mathbf{t}^* \cdot \delta \mathbf{u} dA = 0 & \forall \delta \mathbf{u} \\ f\Psi_0 - \beta f \Delta f - r \leq 0 & \forall \mathbf{x} \in \Omega \end{cases} \tag{22}$$

with the Dirichlet and Neumann boundary conditions $\mathbf{u} = \mathbf{u}^* \forall \mathbf{X} \in \partial\Omega_u$ and $\mathbf{F}\mathbf{S}\mathbf{n}_0 = \mathbf{t}^* \forall \mathbf{X} \in \partial\Omega_\sigma$ with $\partial\Omega = \partial\Omega_u \cup \partial\Omega_\sigma$ and $\partial\Omega \cap \partial\Omega_\sigma = \emptyset$ for (22)₁. For (22)₂, the initial condition $f(t = 0) = 1 \forall \mathbf{X} \in \Omega$ and the Neumann condition $\mathbf{n}_0 \cdot \nabla f = 0 \forall \mathbf{X} \in \partial\Omega$ apply.

From (22)₂, we recognize that a partial differential inequality has to be solved for the primal variable f . Once f is determined, the value of the damage variable could be computed subsequently for each material point \mathbf{X} by $\alpha = -\log[f(\mathbf{X})]$; however, this information is of minor interest. More importantly, the damage function $D = 1 - f$ can be computed which governs the stresses by

$$\mathbf{S} = (1 - D)\mathbf{S}_0 \quad \text{with} \quad \mathbf{S}_0 := 2 \frac{\partial \Psi_0}{\partial \mathbf{C}}. \quad (23)$$

The partial differential inequality in (22)₂ is rather untypical in the context here and a standard finite element treatment would be complex due to the subdifferential in its weak form, compare (13). Furthermore, additional degrees of freedom at the nodes would be present in the numerical solution scheme. To avoid both drawbacks, we follow Reference 32 and make use of the neighbored element method: standard finite element approaches are applied to the weak form of the balance of linear momentum whereas a finite difference approach for unstructured grids is used for discretizing the strong form of the evolution equation for f . The neighbored element method is completed by utilization of an operator split, that is, the discretized equations are solved in a staggered manner. This procedure of combining staggered FEM and FDM has also been proven advantageous for the small-strain regime in Reference 32. In Reference 33, it has been demonstrated that convergence is achieved which justifies the operator split. The finite element treatment of the nonlinear weak form of the balance of linear momentum is standard such that we dispense with a detailed presentation. More details on the finite element method can be found in standard textbooks as in, for example, Reference 42. The only modification is, of course, that both the stress and the stiffness are scaled by the damage state, compare (23). Operator splitting for a phase field approach in damage modeling for linearized kinematics can be found, for example, in Reference 43.

For the derivation of an appropriate finite difference method that also operates on unstructured grids, we employ a Taylor series expansion up to order two in order to approximate f . Usually, the value of the function, that is, its zeroth derivatives, along with the derivatives of higher order are known when a Taylor series expansion is used. Then, due to the chosen spatial increment, the value of the function can be approximated at a neighbored spatial point. This operation is inverted here: the value of the damage function at specific points are all known. These points are the centers of gravity of all finite elements. Then, the spatial increments in the Taylor series expansion are given by the spatial increments of the centers of gravity; they remain fixed if no mesh adaptation is employed during the computation. Consequently, the only unknown in the Taylor series expansion are the (mixed) derivatives of order ≥ 1 . Collecting an appropriate set of neighbored elements, a linear system of algebraic equations can be constructed to compute the individual (partial) derivatives from which the local value of the Laplace operator follows by simple summation of the unmixed derivatives of order two.

Our finite differences approach at unstructured meshes can be recast in mathematical formulas by first introducing the Taylor series expansion as

$$f(\mathcal{N}_k^{(e)}) = f^{(e)} + \sum_o A_o^{(i,k)} f_{\partial,o}^{(e)} \quad (24)$$

where $f_{\partial,o}^{(e)}$ stores the value of the partial derivatives of varying order $o \geq 1$, such that a matrix including all derivatives can be defined as

$$\mathbf{f}_{\partial}^{(e)} := \left(\frac{\partial f^{(e)}}{\partial X} \quad \frac{\partial f^{(e)}}{\partial Y} \quad \frac{\partial f^{(e)}}{\partial Z} \quad \frac{\partial^2 f^{(e)}}{\partial X \partial Y} \quad \frac{\partial^2 f^{(e)}}{\partial Y \partial Z} \quad \frac{\partial^2 f^{(e)}}{\partial X \partial Z} \quad \frac{\partial^2 f^{(e)}}{\partial X^2} \quad \frac{\partial^2 f^{(e)}}{\partial Y^2} \quad \frac{\partial^2 f^{(e)}}{\partial Z^2} \right). \quad (25)$$

The quantity $A_o^{(i,k)}$ comprises all spatial increments with varying power such that again the associated column matrix is defined as

$$\begin{aligned} A^{(k)} := & \left(X_{\Delta}^{(\mathcal{N}_k^{(e)})} \quad Y_{\Delta}^{(\mathcal{N}_k^{(e)})} \quad Z_{\Delta}^{(\mathcal{N}_k^{(e)})} \quad X_{\Delta}^{(\mathcal{N}_k^{(e)})} Y_{\Delta}^{(\mathcal{N}_k^{(e)})} \quad Y_{\Delta}^{(\mathcal{N}_k^{(e)})} Z_{\Delta}^{(\mathcal{N}_k^{(e)})} \quad X_{\Delta}^{(\mathcal{N}_k^{(e)})} Z_{\Delta}^{(\mathcal{N}_k^{(e)})} \right. \\ & \left. \frac{1}{2} \left(X_{\Delta}^{(\mathcal{N}_k^{(e)})} \right)^2 \quad \frac{1}{2} \left(Y_{\Delta}^{(\mathcal{N}_k^{(e)})} \right)^2 \quad \frac{1}{2} \left(Z_{\Delta}^{(\mathcal{N}_k^{(e)})} \right)^2 \right) \end{aligned} \quad (26)$$

with

$$X_{\Delta}^{(\mathcal{N}_k^{(e)})} := X^{(\mathcal{N}_k^{(e)})} - X^{(e)}, \quad Y_{\Delta}^{(\mathcal{N}_k^{(e)})} := Y^{(\mathcal{N}_k^{(e)})} - Y^{(e)}, \quad Z_{\Delta}^{(\mathcal{N}_k^{(e)})} := Z^{(\mathcal{N}_k^{(e)})} - Z^{(e)}.$$

To ensure that only the required number of elements and thus extrapolation points is used, the quantity $\mathcal{N}_k^{(e)}$ has been introduced: $\mathcal{N}^{(e)}$ is the set of neighbored elements around element (e) and, hence, $\mathcal{N}_k^{(e)}$ returns the global element number for k th neighbor. All column matrices $\mathbf{A}^{(k)}$ in the neighborhood $\mathcal{N}_k^{(e)}$ of the element of interest (e) are collected in the matrix $\mathbf{A}^{(e)}$. Then, by defining

$$f_{\Delta,k}^{(e)} := f^{(\mathcal{N}_k^{(e)})} - f^{(e)}, \tag{27}$$

we can shortly write for the Taylor series expansion (24)

$$\mathbf{f}_{\Delta}^{(e)} = \mathbf{A}^{(e)} \mathbf{f}_{\partial}^{(e)} \tag{28}$$

such that the unknown vector of derivatives follows from

$$\mathbf{f}_{\partial}^{(e)} = \mathbf{A}^{(e)-1} \mathbf{f}_{\Delta}^{(e)}. \tag{29}$$

The Laplace operator can be computed by aid of $\mathbf{f}_{\partial}^{(e)}$ according to

$$\Delta f^{(e)} = \frac{\partial^2 f^{(e)}}{\partial X^2} + \frac{\partial^2 f^{(e)}}{\partial Y^2} + \frac{\partial^2 f^{(e)}}{\partial Z^2} = f_{\partial,7}^{(e)} + f_{\partial,8}^{(e)} + f_{\partial,9}^{(e)}, \tag{30}$$

compare (25). Consequently, only some components of $\mathbf{f}_{\partial}^{(e)}$ are of interest. Introducing

$$\mathbf{a} := \begin{pmatrix} 0 & 0 & 0 & 0 & 0 & 0 & 1 & 1 & 1 \end{pmatrix}, \tag{31}$$

the Laplace operator is simply given by

$$\Delta f^{(e)} = \mathbf{l}^{(e)} \cdot \mathbf{f}_{\Delta}^{(e)} \tag{32}$$

where the vector

$$\mathbf{l}^{(e)} := \mathbf{a}^T \mathbf{A}^{(e)-1} \tag{33}$$

can be computed once for each element (e) in advance of the actual solution of the boundary value problem. In contrast, the evaluation of (32) has to be repeated during computational evaluation of (22)₂ to find the (current) field f ; this evaluation, however, is computationally very cheap. It is worth mentioning that the dimension of $\mathbf{A}^{(e)}$ depends on cardinality of the set of neighbored elements $\mathcal{N}^{(e)}$: to close the system of equations in (28), that is, to ensure that $\mathbf{A}^{(e)}$ is a regular matrix, the cardinality of the set of neighbored elements has at least to equal the length of $\mathbf{f}_{\partial}^{(e)} = 9$ in the considered three-dimensional case. For boundary elements, however, we usually find a smaller cardinality of $\mathcal{N}^{(e)}$, that is, less than nine neighbored elements can be identified. To circumvent this problem, we introduce ghost elements at the boundary which mirror the value of the damage field inside of Ω to the outer vicinity of the boundary $\partial\Omega$ which agrees to the usual treatment in the finite difference method. It is worth mentioning that (21) is fulfilled identically by usage of ghost elements. For the elements inside of Ω , the opposite case is present: considering all neighbored elements around (e) in a hexahedra finite element mesh, that is, the stencil of six elements plus eight diagonal elements plus twelve elements in each “plane,” results in an overdetermined system of equations for (28). Here, two possibilities can be employed: the first option is to take into account element (e) and all 26 neighbored elements and compute the inverse of $\mathbf{A}^{(e)}$ by use of the right-inverse as

$$\mathbf{A}^{(e)-1} = \mathbf{A}^{(e)T} (\mathbf{A}^{(e)} \mathbf{A}^{(e)T})^{-1}, \tag{34}$$

compare Reference 33. The second option is to use the six stencil elements plus three diagonal elements with closest distance to the center element (e) as neighborhood. For sufficiently regular meshes, $\mathbf{A}^{(e)}$ contains full rank and is regular, compare Reference 33. In all computational results we present later, we made use of the latter option. We refer to References 32-34 for more details on the neighbored element method. For other types of finite elements, for example, tetrahedra elements, the neighborhood is less intuitively defined than described for hexahedra elements. However, a least squares

approach can be used in this case which replaces the demand of applying the right-inverse. A more detailed investigation of the least squares approach is subject of future investigations.

Finally, it is mandatory to choose a strategy for solving the discretized form of (22)₂ given by

$$\Phi^{(e)} = f^{(e)} \bar{\Psi}_0^{(e)} - \beta f^{(e)} \mathbf{l}^{(e)} \cdot \mathbf{f}_\Delta^{(e)} - r \leq 0 \quad (35)$$

where we introduced the strain energy density averaged for each finite element as

$$\bar{\Psi}_0^{(e)} := \frac{1}{\Omega^{(e)}} \int_{\Omega^{(e)}} \Psi_0 \, dV. \quad (36)$$

The Laplace operator turns (35) into a system of coupled inequalities which could be solved in a monolithic manner. Although being the obvious strategy, the coupling demands the usage of (external) solver routines. In combination with the inequalities, this renders such a monolithic strategy inappropriate to be implemented into an arbitrary finite element program. Therefore, a simple yet successful numerical solution procedure has been proposed in Reference 32: the system of coupled inequalities is solved by means of a Jacobi method. To be more precise, the coupling is ignored at first glance and each inequality is checked individually such that an update of f is performed for all elements with $\Phi^{(e)} > 0$. Of course, a modification of $f^{(e)}$ may have an impact on the indicator function in a different element (k) due to the Laplace operator which “transports” the information. Therefore, the update has to be repeated until $\Phi^{(e)} \leq 0 \, \forall (e)$. Usually, such an update scheme is known to be rather time consuming since the numbers of repetitions needed for convergence depends on the number of unknowns which equals the number of finite elements in our case. This should turn this strategy to be more expensive than monolithic solution schemes. However, the damage evolution is limited to only a small number of elements as compared to their total number and thus, an update is mandatory only for a negligible fraction of inequalities. As will be shown by our numerical experiments, the staggered solution scheme is still very fast and simulations involving damage evolution consume hardly more computation time. A similar behavior has already been demonstrated for the small deformation setting of damage modeling in Reference 32 and even for an evolutionary method for topology optimization both at small strains in Reference 34 and at finite strains in Reference 35. After the damage function has been updated, the next time step is investigated without checking the impact of the updated damage field on the displacements for the current time step. This might be interpreted as (additional) operator step and may seem questionable whether a reliable result is obtained by this method. However, small (but finite) time steps are mandatory for an appropriate resolution for example, of the force/displacement diagram. For this case, the method of operator splits converges. It has been numerically shown in Reference 32 that the artificially included pseudo-viscous behavior due to the operator step does not influence the final result on a relevant scale. Furthermore, it is worth mentioning that a detailed numerical study on the numerical behavior of the damage model for the small deformation setting in Reference 33 revealed that almost identical results are obtained when both fields (displacements and damage) are repeatedly updated until a common convergence is achieved. The update of each inequality is performed by a one-step Newton procedure as

$$f^{(e)} \leftarrow f^{(e)} - \frac{\Phi^{(e)}}{d\Phi^{(e)}} \quad (37)$$

with

$$d\Phi^{(e)} = \Psi_0^{(e)} - \beta \mathbf{l}^{(e)} \cdot \mathbf{f}_\Delta^{(e)} + \beta f^{(e)} \mathbf{l}^{(e)} \cdot \mathbf{1} \quad (38)$$

where the length of the vector $\mathbf{1}$ equals the cardinality of the set $\mathcal{N}^{(e)}$ (9 for our chosen method for defining the neighborhood) and all elements in $\mathbf{1}$ are set to one. The one-step Newton method has been proven beneficial due to its smooth convergence behavior for neighbored elements caused by the undershooting. Additionally, this ensures a monotonic decrease of the damage function and thus agrees to (20)₁: the indicator function $\Phi^{(e)}$ is a convex quadratic function in $f^{(e)}$, and since the update for $f^{(e)}$ is only performed for $\Phi^{(e)} > 0$, it holds for the derivative $d\Phi^{(e)} > 0$. The undershooting ensures that the solution converges from above, that is, $0 \leftarrow \Phi^{(e)}$, and thus $f^{(e)}$ is monotonically decreasing which implies $\dot{\alpha} \geq 0$.

The above mentioned numerical procedure is analogous to the one used for the small deformation setting in Reference 32. However, a remarkable difference is accompanied by the large deformation setting: here, severe deformations that occur during damage evolution are correctly described. This, of course, is the primal intention of using

Algorithm 1. Element erosion strategy

```

for  $1, \dots, n_e$  do                                     ▷ apply to all finite elements
    if  $D^{(e)} = D_{\text{crit}}$  then                               ▷ check damage criterion
        set  $\mathbf{r}^{(e)} = \mathbf{0}$                                ▷ eliminate element residual
        set  $\frac{d\mathbf{r}^{(e)}}{d\hat{\mathbf{u}}^{(e)}} = \left( \frac{dr_i^{(e)}}{d\hat{u}_j^{(e)}} \right) = s_{\text{crit}}(\delta_{ij})$            ▷ erode element ( $e$ )
    end if
end for

```

the large deformation setting. Unfortunately, this sensitivity might result in numerical instabilities causing $\det \bar{\mathbf{F}}^{(e)} < 0$ where $\bar{\mathbf{F}}^{(e)} := \int_{\Omega^{(e)}} \mathbf{F} dV / \Omega^{(e)}$ is the averaged deformation gradient in element (e). To be more precise, deformation states are computed that do not correspond to a physically accurate material behavior: once the deformation state has reached some critical threshold, cracks will be present in a real material such that a consideration of the specimen as one continuous body cannot be justified and a description in a continuum mechanical sense is not justified anymore. To circumvent this numerical artifact and also to improve physical accuracy, a stabilization technique in terms of element erosion is applied. To this end, we define a critical value D_{crit} when damage modeling is not suitable anymore but rather cracking needs to be considered. To correctly account for this physical behavior in our finite element simulations, we thus modify the element stiffness by setting it to a diagonal matrix with a virtual remaining stiffness value of s_{crit} representing an eroded element through which rank deficiency of the affected elements is avoided. Finally, we set the residual forces of this element to zero and no further evolution of the damage value is considered anymore at this point such that eroded elements make use of value $f_{\text{crit}} = 1 - D_{\text{crit}}$. Consequently, the presented neighbored element method is directly applicable in combination with the element erosion technique: eroded elements simply possess a (constant) value $f = f_{\text{crit}}$ which is small but finite. Thus, the finite difference scheme which is employed for the computation of f also operates in a smooth manner when combined with the element erosion strategy which solely modifies the finite element method as presented.

Remark: the application of the erosion technique is not mandatory for moderate deformation states when a finite element description of the cracking is still valid. Only when severe damage has been evolved which causes the damaged finite element to loose its validity as is the case, for instance, for wide crack opening the erosion approach needs to be activated. An important subproblem is the case of self-contact of the crack surfaces when the external load is removed again. In this case, the finite elements containing damage are still present in the mesh but they are only numerical artifacts with no relevant information or influence on the simulation. For the contact situation, the contact surfaces need to be identified appropriately. Here, a re-meshing once the loading is reduced seems to be a suitable treatment to remove the eroded finite elements completely from the mesh and to subsequently identify the contact areas. However, a detailed investigation of this problem is beyond the scope of the current manuscript and will be part of future research.

Summarizing, we follow the element erosion technique in Algorithm 1 and employ Algorithm 2 for the damage update. The flowchart in Figure 1 visualizes the neighbored element approach including an interplay between a finite element and finite difference update for the displacements and f , respectively.

4 | NUMERICAL TESTS

In this section, the introduced approach is numerically tested in a 3D finite strain setting. To this end, corresponding 8-node hexahedral finite elements were implemented and evaluated within the finite element program FEAP, compare Reference 44. For the strain energy corresponding to the fictively undamaged state, the Neo-Hooke energy given as

$$\Psi_0 = \frac{\mu}{2}(I - 3) + g(J) \quad (39)$$

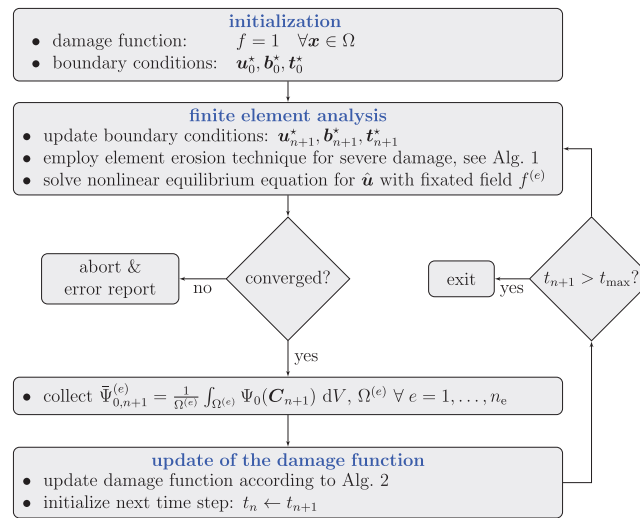


FIGURE 1 Flowchart for the proposed damage model

TABLE 1 Material and boundary parameters used throughout the numerical tests

Description	Symbol	Value		Unit
		Plate with hole	U-shape	
E-modulus	E	500	1000	MPa
Poisson ratio	ν	0.3	0.3	-
Dissipation parameter	r	5.0	0.5	MPa
Nonlocal parameter	β	$\in \{10, 100, 1000\}$	100	N
Critical damage value	D_{crit}	0.95	0.995	-
Critical stiffness	s_{crit}	10^{-8}	10^{-8}	N/mm
Load increment	-	$\{0.025, 0.01, 0.0025\}$	0.2	mm

with $g(J) = \frac{\lambda}{4}(J^2 - 1) - \left(\frac{\lambda}{4} + \mu\right) \ln J$ and $I = \text{tr}[\mathbf{C}]$, $J = \det \mathbf{F}$ is employed (see also Reference 42). The Lamé constants $\lambda = E\nu/((1 + \nu)(1 - 2\nu))$ and $\mu = E/(2(1 + \nu))$ are computed from the Young's modulus E and the Poisson ratio ν . Throughout the numerical tests, an element erosion approach is incorporated as discussed in Section 3 through which, once the damage value of an element exceeds a critical value $D^{(e)} > D_{\text{crit}}$, the element stiffness is replaced by a virtual remaining stiffness s_{crit} and residual forces are eliminated, compare alg. 1. Moreover, to avoid damage evolution under compression, we add the condition $\det \bar{\mathbf{F}}^{(e)} > 1$ to the damage update algorithm in Algorithm 2. For the solution procedure uniform incremental loading is applied and the solution of the linearized system corresponding to the Newton–Raphson iterations is performed with the PARDISO solver. The parameters for the technique for element erosion are collected in Table 1.

4.1 | Plate with hole benchmark test

As first example, we consider a plate with a circular hole which is subjected to the prescribed displacement $\mathbf{u}^* = (0, u^*, 0)^T$ with $u^* = 25$ mm at its upper boundary ($Y = L$, with $L = 100$ mm). The geometry of the considered domain is depicted in Figure 2A. Due to the symmetry of the problem, the computational domain amounts only to the upper right quarter of the geometry. Moreover, as a consequence of the symmetry, the displacement is fixed in X-direction with $u_x = 0$ at the left edge $X = 0$ and in Y-direction with $u_y = 0$ at the lower edge $Y = 0$. The radius of the circular hole as shown in Figure 2A is given with $R = 50$ mm and the thickness is given with $H = 10$ mm. An overview of the used material and load parameters is collected in Table 1.

Algorithm 2. Damage update

```

input  $\bar{\Psi}_{0,n+1}^{(e)} = \int_{\Omega^{(e)}} \Psi_{0,n+1} dV / \Omega^{(e)}$  ▷ averaged energy for each finite element ( $e$ )
 $\bar{\mathbf{F}}^{(e)} = \int_{\Omega^{(e)}} \mathbf{F} dV / \Omega^{(e)}$  ▷ averaged deformation gradient for each element ( $e$ )

for  $1, \dots, n_{\text{loop}}$  do ▷ Jacobi method: repeat  $n_{\text{loop}}$  times

  compute  $\Delta f^{(e)}$  according to (32) ▷ Laplace operator

  compute  $\Phi^{(e)}$  according to (35) ▷ indicator function

  if  $\Phi^{(e)} > 0$  and  $\det \bar{\mathbf{F}}^{(e)} > 1$  then
    update  $f^{(e)} \leftarrow f^{(e)} - \frac{f^{(e)}}{d\Phi}$  according to (38) ▷ new damage value for inelastic  $\Phi^{(e)}$ 

    if  $D^{(e)} = 1 - f^{(e)} > D_{\text{crit}}$  then
      set  $D^{(e)} = D_{\text{crit}}$  and  $f^{(e)} = 1 - D_{\text{crit}}$  ▷ activation of element erosion
    end if

  else
    set  $\Phi^{(e)} = 0$  ▷ elimination of elastic  $\Phi^{(e)}$ 
  end if

  if  $\max\{\Phi^{(e)}\} < 10^{-6}$  then
    exit ▷ terminate Jacobi method
  end if
end for

```

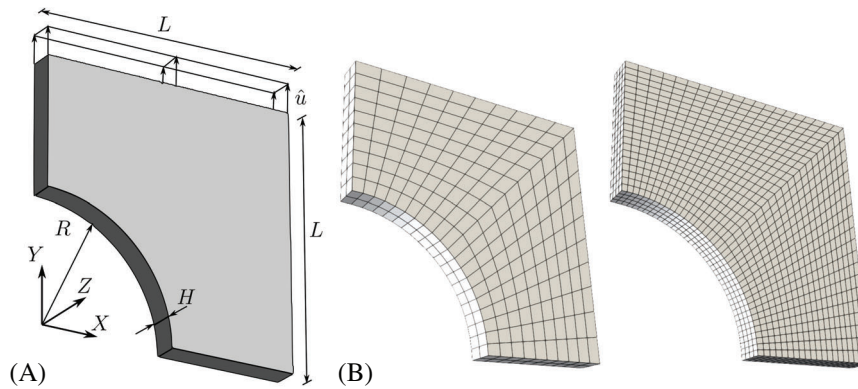


FIGURE 2 (A) Description of the geometry of the plate with hole benchmark problem. (B) Example finite element meshes (400 and 3200 elements)

4.1.1 | Convergence study

In Figures 3A and 4A, force/displacement curves corresponding to various mesh refinements (see e.g., Figure 2B) are shown. The value of the prescribed displacement u^* is depicted on the abscissa whereas the value of the reaction force F in Y -direction, which is recovered from the nodes at the upper surface $Y = L$, is plotted on the ordinate. Here, the non-local parameter has the value $\beta = 100 \text{ N}$. For the results presented in Figure 3, the prescribed displacement is applied in increments of 0.025 mm, which is equivalent to 1000 load steps. In order to compare results for varying stepsize, the same problem is analyzed for a refined stepsize in Figure 4 where the prescribed displacement is applied in increments of 0.01 mm which is equivalent to 2500 load steps. For the given plot resolution both in Figures 3A and 4A, it can be

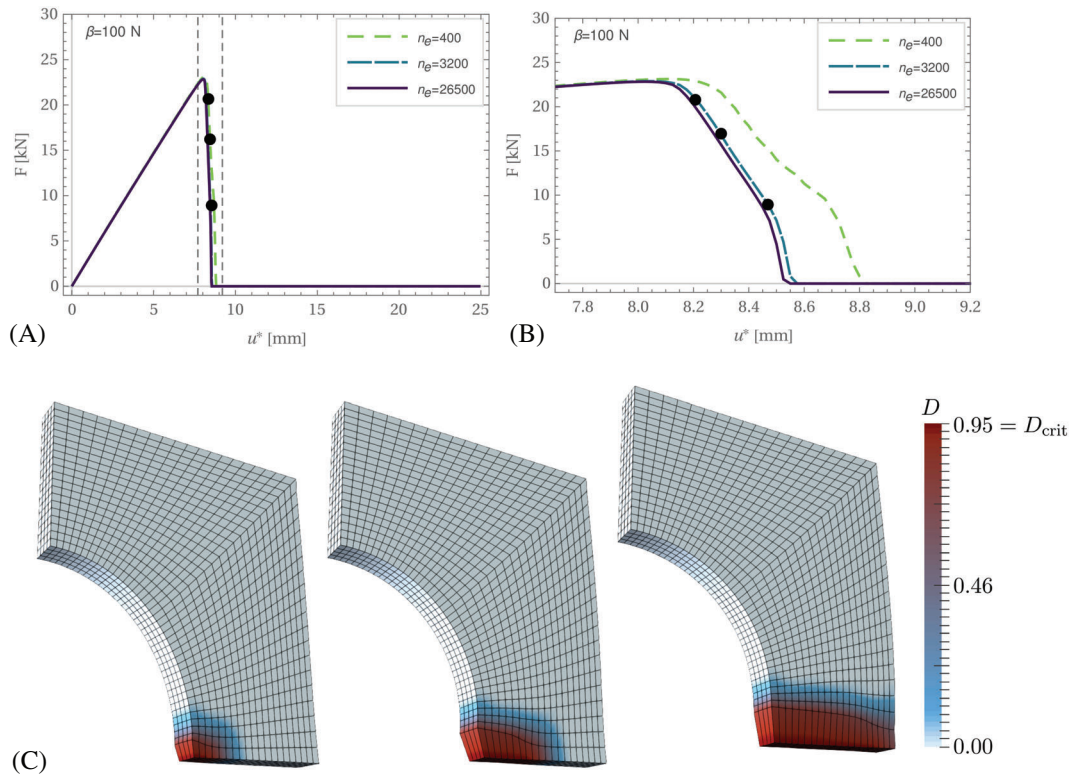


FIGURE 3 (A) Force/displacement curves (higher resolution in (B)) and (C) corresponding contourplots depicting the damage evolution for the 3200 element mesh in three different load steps which are depicted as bullets in (A). The load increment is 0.025 mm

observed that the force/displacement curves of the lower refinement stage (400 elements) almost coincide with the curves corresponding to the higher refinement stages. Thus, to illustrate the convergence of the curves as the number of elements increases, an enlarged resolution of the plot is given in Figures 3B and 4B. The area of the enlargement is the transition regime at which material softening occurs (marked with gray dashed lines in the corresponding left-hand side figures). The evolution of the material softening is also illustrated through the contourplots of the damage function D in Figures 3C and 4C. The contourplots correspond to the computation with the 3200 element mesh and the depicted stages of damage evolution are marked with bullets in the corresponding force displacement curves. It can be observed that already at low damage propagation states, as depicted in the left contourplot, the damage value D of several elements reaches the critical damage value D_{crit} . Furthermore, when comparing Figures 3 and 4, which depict the same convergence study but with varying stepsize (0.025 and 0.01 mm respectively), a similar behavior with respect to mesh independency and damage evolution can be observed. For all computations, convergence of the iterative solution procedure was obtained.

4.1.2 | Influence of the nonlocal parameter

In this subsection, the influence of the value of the nonlocal parameter β on the convergence behavior and the damage evolution is investigated. Therefore, in Figure 5 corresponding force/displacement curves are shown for values $\beta = 10, 100$, and 1000 N, respectively. A load increment of 0.025 mm is used and the computations are performed on a 400 (Figure 5A) and a 3200 (Figure 5B) element mesh. It can be observed that the starting point of damage initialization is shifted to higher load values as β increases. This goes along with the increased nonlocality of the distribution of the damage function D as depicted in the contourplots of Figure 5C: while in the left contourplot ($\beta = 10$ N) the damage distribution is mostly concentrated to the elements adjacent to the lower edge, in the right contourplot ($\beta = 1000$ N), a more smeared damage distribution can be observed.

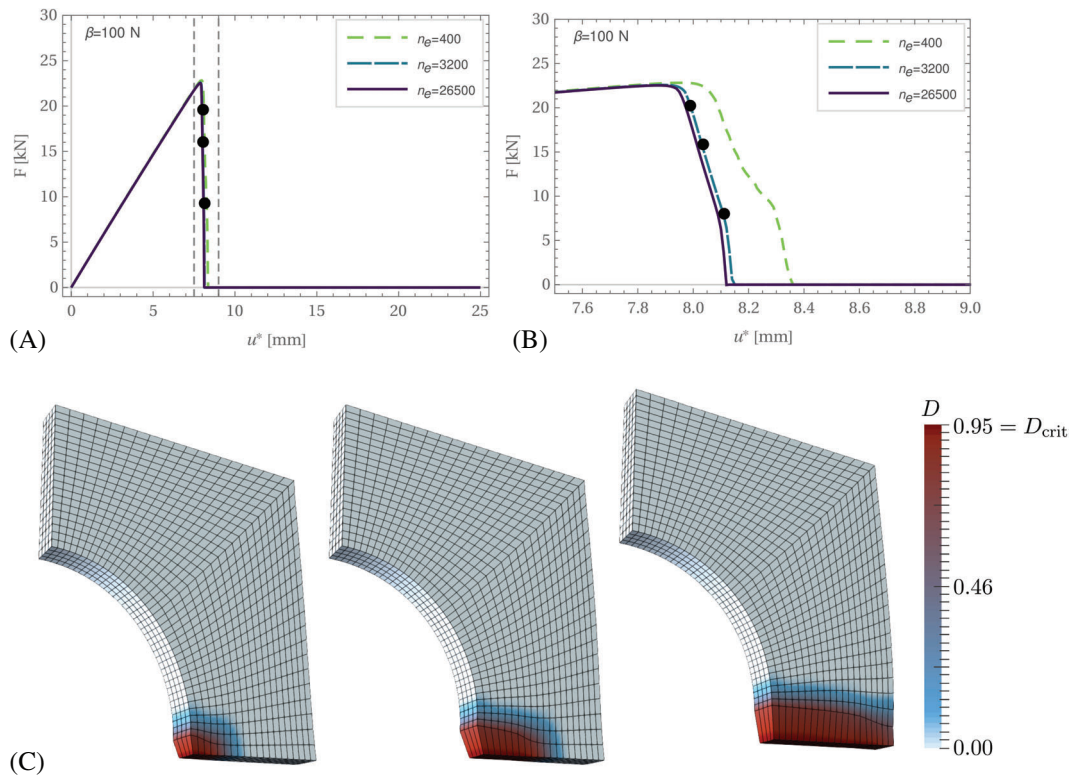


FIGURE 4 (A) Force/displacement curves (higher resolution in (B)) and (C) corresponding contourplots depicting the damage evolution for the 3200 element mesh in three different load steps which are depicted as bullets in (A). The load increment is 0.01 mm

4.1.3 | Influence of the load increment and computing efficiency

To investigate the influence of the load increment on the solution, we show the convergence of the force/displacement curves for the specific displacement increments $\{0.25, 0.1, 0.025, 0.01\}$ mm, while the mesh refinement stage (400 elements) and nonlocal parameter ($\beta = 1000$ N) remain fixed. We expect a sudden failure due to the perfectly brittle material behavior. In a numerical sense, this corresponds to a complete loss of the reaction force which takes place in a minimal number of load steps after damage initiation. In the limit, total failure is established in only one single load step. However, the limit case is approximated by a small number of load steps due to the operator split. For the chosen parameters, the corresponding curves are depicted in Figure 6A and converge to the expected vertical branch during brittle failure which is resolved better as the value of the load increment decreases and, consequently, the number of steps increases. It is worth mentioning that the proper resolution of the vertical branch caused by rapid damage evolution is more challenging to be numerically handled than a slower damage evolution with a less steep decrease of the reaction force. For this reason, we do not present numerical results for a modified model including an increasing dissipation parameter $r(\alpha)$ with reduced damage evolution.

Remark: the material model is based, as usual for displaying damage, on a non-convex mechanical energy $(1 - D(\alpha))\Psi_0(\mathbf{C})$. Furthermore, we make use of a dissipation function of order one. The result is an evolution equation without a transient term which would allow for a control of the evolution velocity of the damage. A transient term, which could be included by adding an additional term to the dissipation function which is homogeneous of order two, converts the stationarity condition and thus the Hamilton functional being explicitly time-dependent. An appropriate choice of the viscosity then allows to control the velocity of damage evolution. This property is used by time-wise regularization as, for instance, in Reference 17. The slope of the force/reaction curve could be controlled by choosing $r = r(\alpha)$ as discussed also above.

Remark: Here, we present results for prescribed displacements which monotonically increase. Therefore, the force/displacement curve is bijective. This, in particular, implies that no snapback can be observed. The characteristic surjectivity in snapback phenomena demands the parameterization of the curve, that is, in terms of the process time. Then,

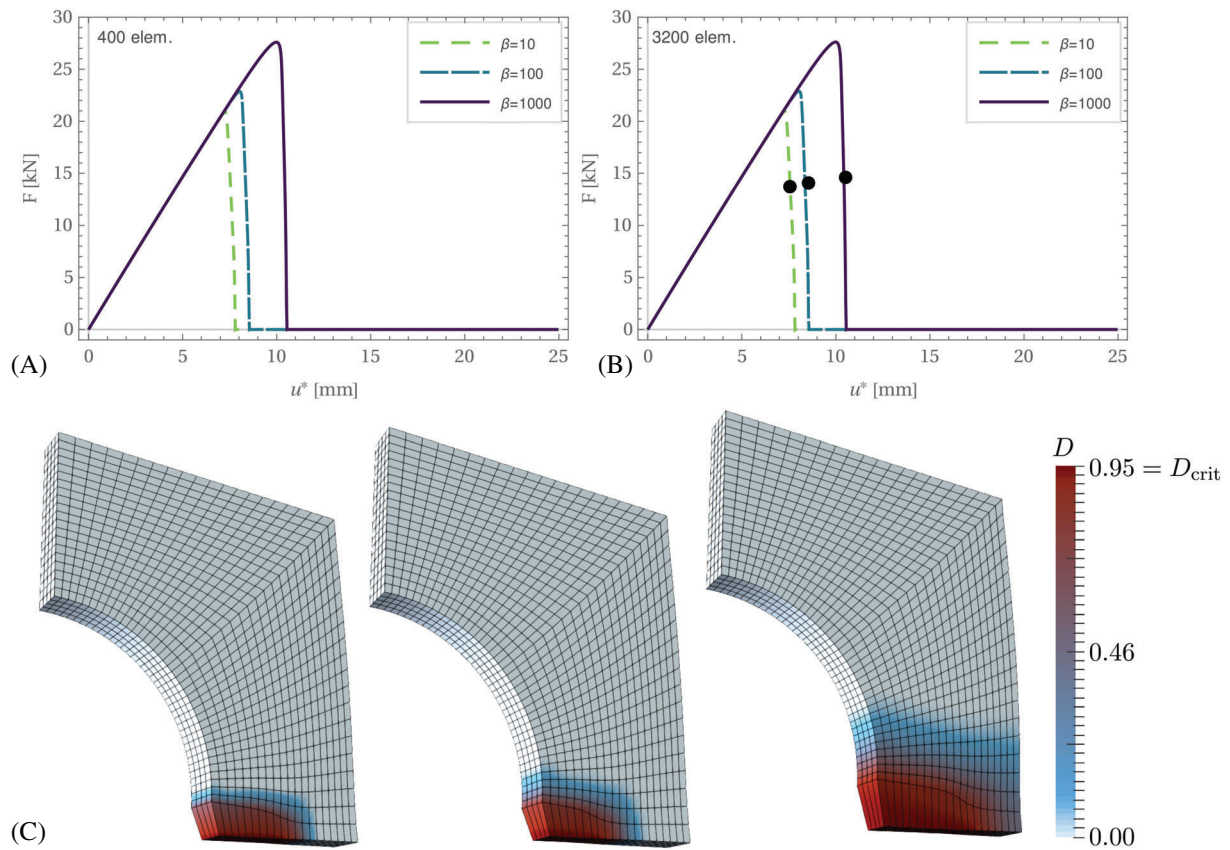


FIGURE 5 Influence of the nonlocal parameter: force/displacement curves for varying nonlocal parameters corresponding to computations with a stepsize of 0.025 mm and a coarse mesh with 400 elements in (A) and a finer mesh with 3200 elements in (B). (C) Contourplots corresponding to the bullet marks in (B). Left: $\beta = 10$ N, center: $\beta = 100$ N, right: $\beta = 1000$ N

an arc length scheme can be employed. The respective behavior including arc length control and resulting snapback is presented in Figure 7.

Furthermore, Figure 6B shows the computing time for the gradient damage model (labeled with GD) and a comparative purely elastic simulation (labeled with EL). The time is measured until the crack has completely evolved which corresponds to a load of $u^* = 10.85$ mm. Considering also later loading steps would result in an overestimation of the computation time of the elastic simulation: whereas for the elastic material behavior a non-linear finite element simulation has to be performed which requires more than two iteration steps for convergence, the damage model has to solve the rigid body movement due to the completely evolved horizontal crack that separated the plate. Consequently, only two iteration steps are required for convergence yielding a total computing time that is larger for the elastic problem than for the damage model. The elastic problem has been solved by deactivating the update subroutine for the damage field. This implies that the same effort for writing the results to text files was needed and no unfair acceleration of either simulation has been employed. For reaching the critical load of $u^* = 10.85$ mm, the elastic simulation required $t = 154.9$ s while the damage simulation finished after $t = 159.8$ s. This computing time increase of 3.2 % of the proposed approach compared to the purely elastic reference simulation unveils that the additional time corresponding to the damage update represents only a small portion of the overall computing time. For instance, if instead a full finite element scheme for the balance of linear momentum as well as for the microstructure evolution leading to four nodal unknowns is employed, the computation costs time can easily be a multiple of the computing time required for the purely hyperelastic problem. A comparable observation has also been made for the evaluation of the damage model in the context of small deformations in Reference 32. The results of a comparative computation are shown in Figure 6C,D. Here, a more refined mesh (3200 elements) and stepsize (0.01 mm) and a nonlocal parameter $\beta = 100$ N is used. Again the computing time is compared to a corresponding purely elastic computation. As expected, a higher overall computing time ($t = 2712.42$ s) for reaching the rupture point ($u^* = 8.16$) mm can be observed for this larger problem size. However, the relative increase in computing time of the gradient damage formulation compared to the elastic reference configuration ($t = 2431.05$ s) remains

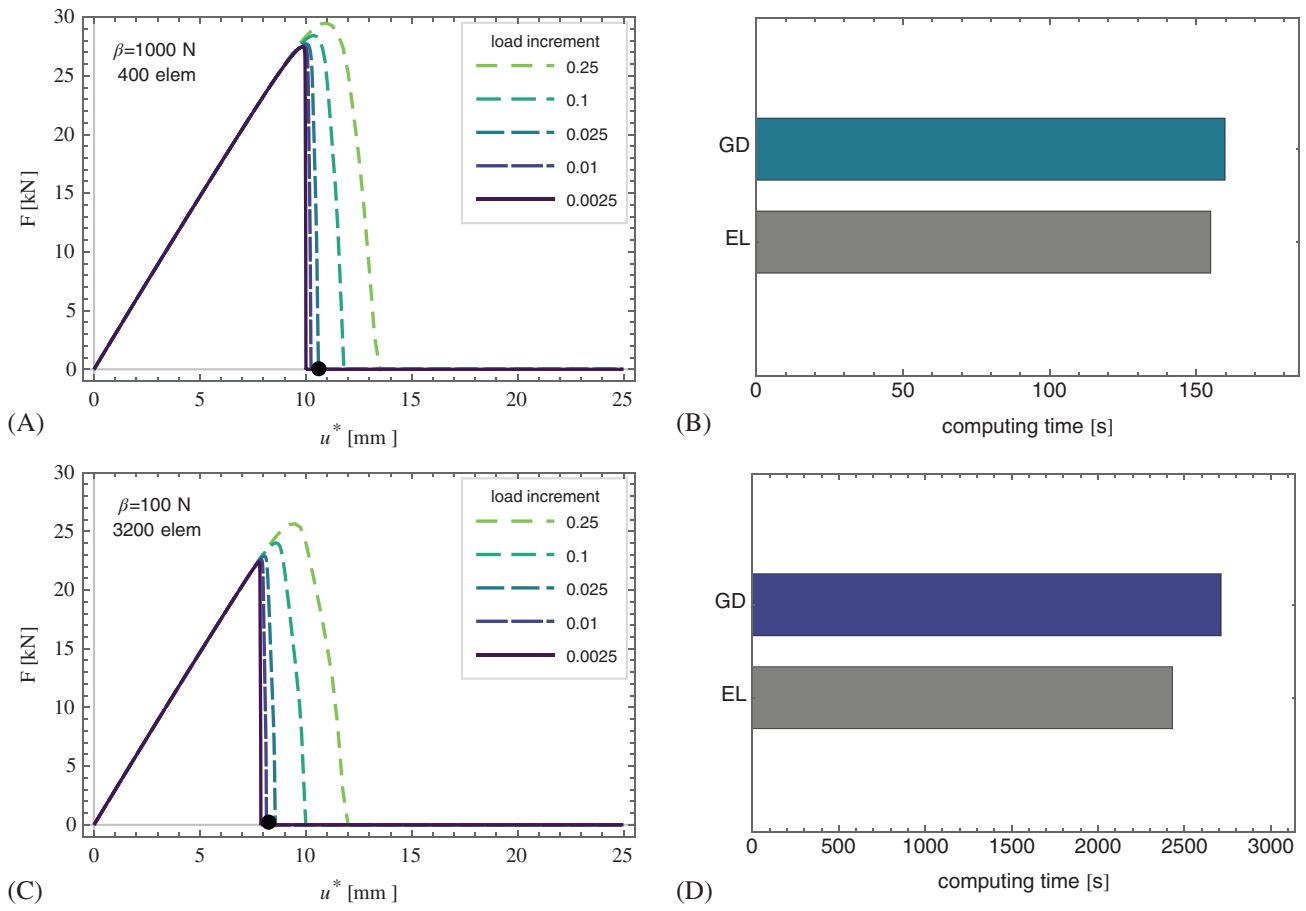


FIGURE 6 (A) Influence of the load increment on the solution: force/displacement curves for varying load increments for a 400 element mesh and $\beta = 1000$ N. (B) GD: computing time until reaching the marked point at $u^* = 10.85$ mm in (A) with the load increment 0.025 mm. EL: computing time of a purely elastic 8-node hexahedral reference element until the same load of $u^* = 10.85$ mm. (C) Force/displacement curves for varying load increments for a 3200 element mesh and $\beta = 100$ N. (D) Computing time until reaching the marked point at $u^* = 8.575$ mm in (C) with the load increment 0.01 mm

relatively small (11.2% increased computation time). A collection of the computation times for the damage model (GD) and elastic simulations for varying mesh sizes and load steps is given in Table 2. The extent of the limited computational extra effort for the gradient-enhanced damage model in comparison to reference hyperelastic simulations is, to the best of our knowledge, a unique feature of our approach.

We present the behavior of the model when employing arc length control in Figure 7. For the arc length control, the equation

$$s = l \sqrt{\sum_i^n \Delta \hat{f}_i^2 + c \sum_i^n \Delta \hat{u}_i^2} \tag{40}$$

is added to the discrete global system of equations which replaces the boundary condition with prescribed displacements u_Y^* at $Y = L$. Here, s is the prescribed increment of the arc length of the force/displacement curve and n is the number of nodes with imprecise boundary conditions. To be more precise, the boundary conditions are not explicitly stated as, for instance, in our other results which are displacement-controlled. In contrast, by prescribing s , the total change of the displacements and reaction forces at the boundary is controlled as specified in (40) where l is the updated arc length and c is a scaling factor (cf. Reference 44). Due to this modification of the boundary condition for the corresponding force displacement curves in Figure 7A (enlargement in Figure 7B), the snapback behavior can be observed. Corresponding contourplots are shown in Figure 7C and visualize the damage evolution for various load stages.

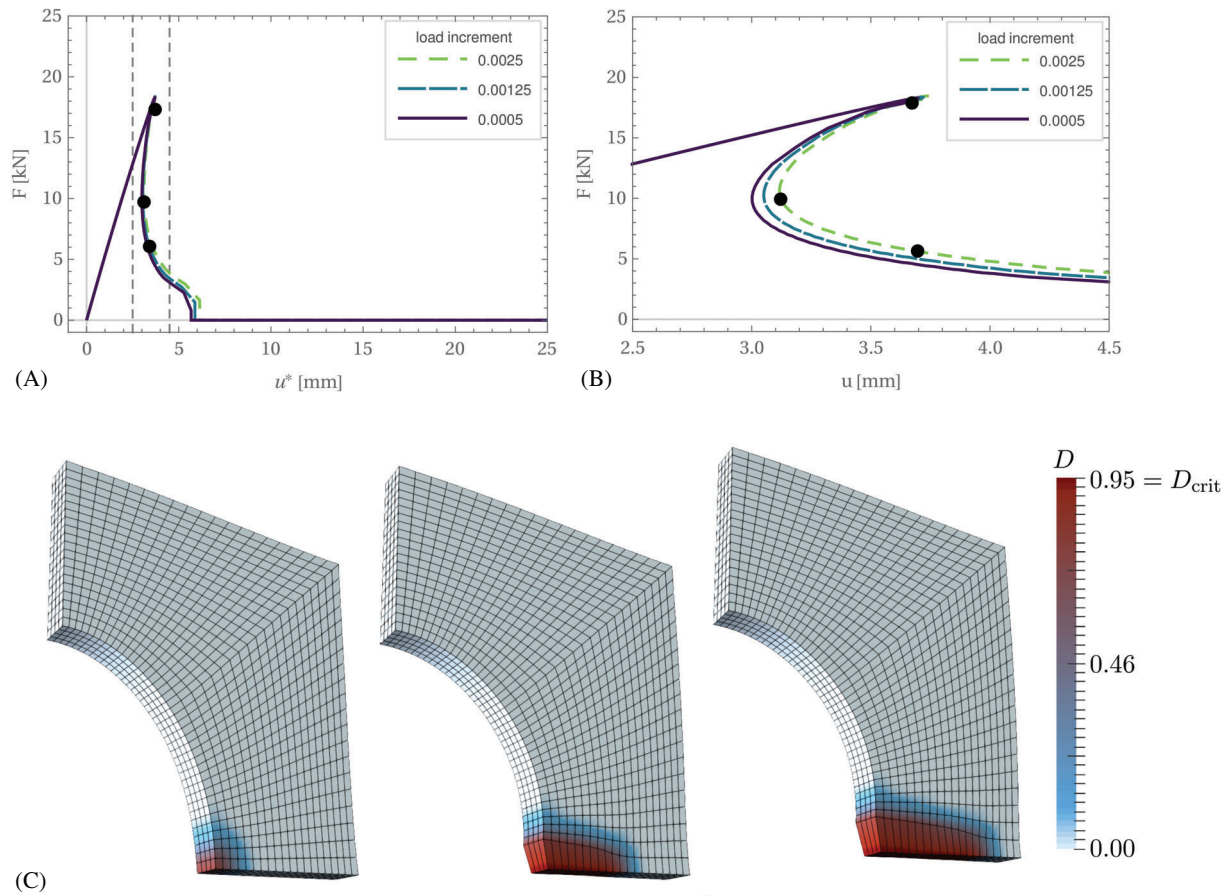


FIGURE 7 Comparative computation employing arc length control. (A): Force/displacement curves for varying load increments for a 25,600 element mesh and $\beta = 100$ N (higher resolution in (B)). (C): Contourplots depicting the damage evolution for a 3200 element mesh computation with 0.0025 load increment solution corresponding to the load stages marked with bullets in (A) and (B)

TABLE 2 Overview of computing times (GD) of the plate with hole benchmark problem relative to a purely elastic reference computation (EL)

	1000 steps			2500 steps		
	EL	GD	% incr.	EL	GD	% incr.
400 elem., $\beta = 1000$ N	154.9s	159.8s	3.2%	322.23s	344.52s	6.9%
3200 elem., $\beta = 100$ N	1109.78s	1177.98s	6.1%	2431.05s	2712.05s	11.6%

Note: Evaluated is the computing time at reaching the loadstep at which the damage computations reach complete failure (cf. bullet marks in Figure 6A,C).

4.2 | U-shaped geometry

As second numerical test, a u-shaped geometry is analyzed in which, caused by its geometry and boundary conditions, large deformations are present (cf. Figure 8A) although the strains may be comparatively moderate. Due to its symmetry, only the left half of the domain is considered and the displacement $u_x = 0$ is fixed at the symmetry plane $X = 0$. The dimensions (cf. Figure 8A) are given with $R = 50$ mm and $S = 10$ mm. The prescribed displacement $\mathbf{u}^* = (u^*, 0, 0)$ with $u^* = 100$ mm is imposed on the upper right edge $(X, Y) = (-50, 50)$ mm. The used material and boundary parameters are shown in Table 1. From the force/displacement curves shown in the upper plot in Figure 8B and with refined resolution in the lower figure, convergence can be concluded. Due to the relatively large displacement, the additional material nonlinearity becomes visible in the force/displacement curves (pile-up of the reaction force close to failure). The contourplots in Figure 8C illustrate the damage propagation at the load stages marked with bullets in the

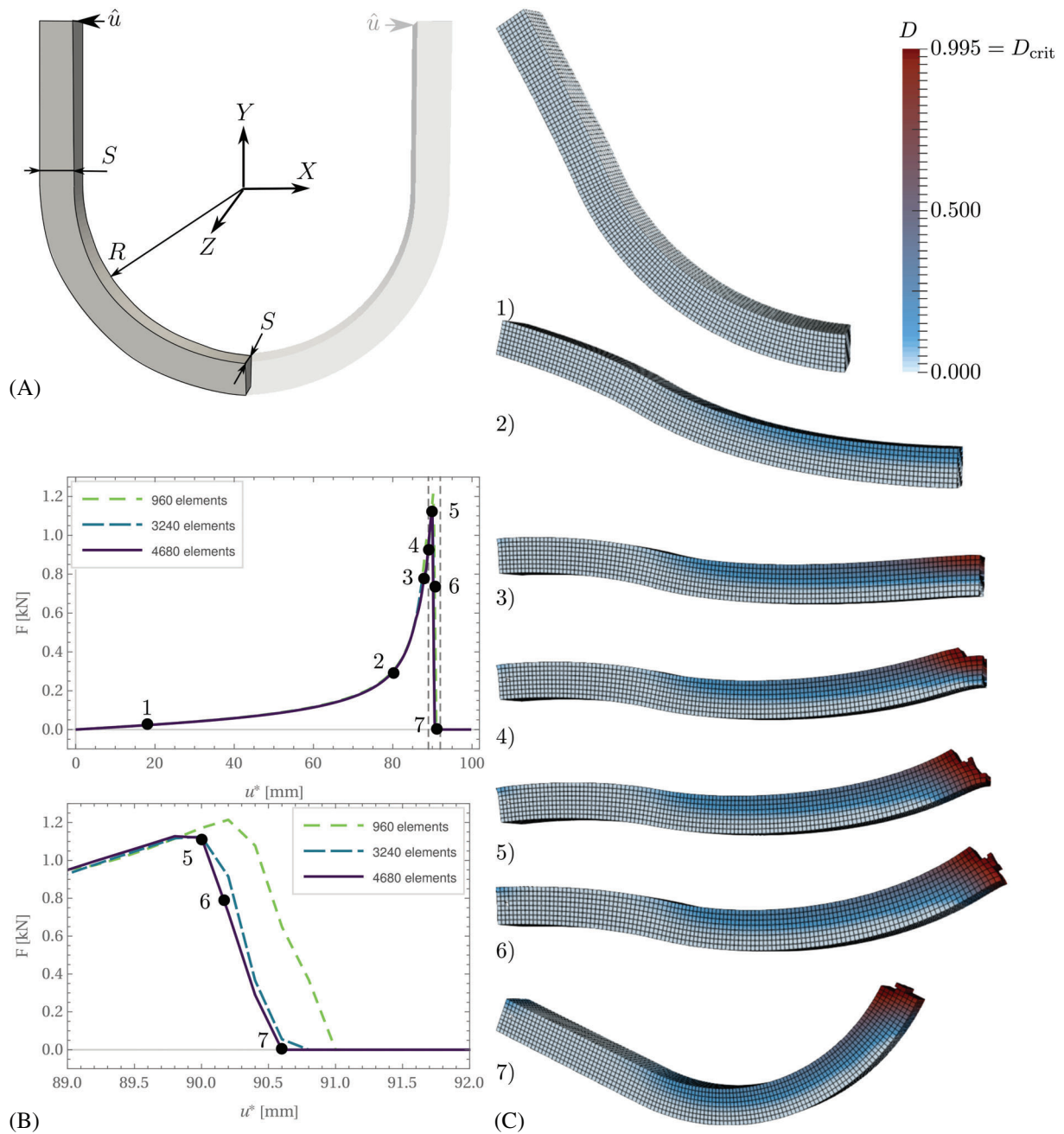


FIGURE 8 (A) Description of the geometry of the u-shaped boundary value problem. (B) Force/displacement curves for various mesh refinement stages (enlarged resolution in the bottom). (C) Contourplots of the u-shaped problem visualizing the damage evolution corresponding to the marked load stages depicting the damage evolution

force/displacement plots. Here, to visualize the crack formation in the entirely damaged area of the domain, the elements in which the damage value has reached the upper bound $D^{(e)} = D_{crit} = 0.995$ were made invisible. A remarkable elastic springback effect is observed once the geometry fails, compare Figure 8C7). Despite the relatively coarse time discretization, convergence of the iterative solution was obtained at all refinement stages. It is worth mentioning that the springback phenomenon constitutes a non-trivial process in a numerical treatment. Since we also observe convergence for this regime, the u-shaped boundary value problem empirically shows the numerical robustness of our approach to damage modeling for large deformations. This example thus serves as benchmark problem which allows to attribute a high numerical robustness to our model and numerical treatment (neighborhood element method combined with the element erosion technique).

5 | CONCLUSIONS

We presented a novel gradient damage model for hyperelastic structures undergoing large deformation along with an efficient and stable numerical update scheme. Numerical results showed convergence for varying mesh size and increasing regularization parameter β . For a smooth iterative solution scheme, it was necessary to develop a stabilization technique that allows for erosion of finite elements with damage exceeding a critical damage state without the need of remeshing. Concluding, we obtained an efficient numerical approach for damage processes to be described in the large deformation setting. In future investigations, important physical aspects like plasticity and hardening will be included.

ACKNOWLEDGMENT


The authors Johannes Riesselmann and Daniel Balzani greatly appreciate funding by the German Science Foundation (Deutsche Forschungsgemeinschaft, DFG) as part of the Priority Program German 1748 “Reliable simulation techniques in solid mechanics. Development of non-standard discretization methods, mechanical and mathematical analysis,” project ID BA2823/15-1.


DATA AVAILABILITY STATEMENT

The data that support the findings of this study are available from the corresponding author, Philipp Junker, upon reasonable request.

ORCID

Philipp Junker  <https://orcid.org/0000-0002-8572-6841>

Johannes Riesselmann  <https://orcid.org/0000-0001-9080-1634>

Daniel Balzani  <https://orcid.org/0000-0002-1422-4262>

REFERENCES

1. Bažant ZP, Jirásek M. Nonlocal integral formulations of plasticity and damage: survey of progress. *J Eng Mech.* 2002;128(11):1119-1149.
2. Peerlings RHJ, Geers MGD, de Borst R, Brekelmans WAM. A critical comparison of nonlocal and gradient-enhanced softening continua. *Int J Solids Struct.* 2001;38(44):7723-7746.
3. Forest S, Lorentz E. Localization phenomena and regularization methods. *Local Approach Fract.* 2004;1:311-371.
4. Yang Y, Misra A. Micromechanics based second gradient continuum theory for shear band modeling in cohesive granular materials following damage elasticity. *Int J Solids Struct.* 2012;49(18):2500-2514.
5. Ortiz M, Stainier L. The variational formulation of viscoplastic constitutive updates. *Comput Methods Appl Mech Eng.* 1999;171(3-4):419-444.
6. Mielke A. Energetic formulation of multiplicative Elasto-plasticity using dissipation distances. *Contin Mech Thermodyn.* 2003;15(4):351-382.
7. Hackl K, Mielke A, Mittenhuber D. Dissipation distances in multiplicative elastoplasticity. In: Wendland W, Efendiev M, eds. *Analysis and Simulation of Multifield problems. Lecture Notes in Applied and Computational Mechanics.* Vol 12. Springer; 2003:87-100.
8. Miehe C. Strain-driven homogenization of inelastic microstructures and composites based on an incremental variational formulation. *Int J Numer Methods Eng.* 2002;55(11):1285-1322.
9. Gürses E, Miehe C. On evolving deformation microstructures in non-convex partially damaged solids. *J Mech Phys Solids.* 2011;59(6):1268-1290.
10. Balzani D, Ortiz M. Relaxed incremental variational formulation for damage at large strains with application to fiber-reinforced materials and materials with truss-like microstructures. *Int J Numer Methods Eng.* 2012;92(6):551-570.
11. Schmidt T, Balzani D. Relaxed incremental variational approach for the modeling of damage-induced stress hysteresis in arterial walls. *J Mech Behav Biomed Mater.* 2016;58:149-162.
12. Schwarz S, Junker P, Hackl K. Variational regularization of damage models based on the emulated RVE. *Contin Mech Thermodyn.* 2020;1-27.
13. Faria R, Oliver J, Cervera M. A strain-based plastic viscous-damage model for massive concrete structures. *Int J Solids Struct.* 1998;35(14):1533-1558.
14. Needleman A. Material rate dependence and mesh sensitivity in localization problems. *Comput Methods Appl Mech Eng.* 1988;67:69-85.
15. Suffis A, Lubrecht TA, Combescure A. Damage model with delay effect: Analytical and numerical studies of the evolution of the characteristic damage length. *Int J Solids Struct.* 2003;40(13-14):3463-3476.
16. Junker P, Schwarz S, Makowski J, Hackl K. A relaxation-based approach to damage modeling. *Contin Mech Thermodyn.* 2017;29:291-310.
17. Langenfeld K, Junker P, Mosler J. Quasi-brittle damage modeling based on incremental energy relaxation combined with a viscous-type regularization. *Contin Mech Thermodyn.* 2018;30(5):1125-1144.
18. de Borst R. Some recent issues in computational failure mechanics. *Int J Numer Methods Eng.* 2001;52(1-2):63-95.

19. Peerlings RHJ, de Borst R, Breckelmans AM, de Vree JHP. Gradient enhanced damage for quasi-brittle materials. *Int J Numer Methods Eng*. 1996;39:3391-3403.
20. Peerlings R, Massart TJ, Geers MGD. A thermodynamically motivated implicit gradient damage framework and its application to brick masonry cracking. *Comp Methods Appl Mech Eng*. 2003;193:3403-3417.
21. Dimitrijevic B, Hackl K. A method for gradient enhancement of continuum damage models. *Tech Mech*. 2008;28(1):43-52.
22. Gross D, Seelig T. *Fracture Mechanics: With an Introduction to Micromechanics*. Springer; 2017.
23. Kiefer B, Waffenschmidt T, Sprave L, Menzel A. A gradient-enhanced damage model coupled to plasticity-multi-surface formulation and algorithmic concepts. *Int J Damage Mech*. 2018;27(2):253-295.
24. Miehe C, Aldakheel F, Raina A. Phase field modeling of ductile fracture at finite strains: a variational gradient-extended plasticity-damage theory. *Int J Plast*. 2016;84:1-32.
25. Ambati M, Kruse R, De Lorenzis L. A phase-field model for ductile fracture at finite strains and its experimental verification. *Comput Mech*. 2016;57(1):149-167.
26. Carollo V, Reinoso J, Paggi M. A 3D finite strain model for intralayer and interlayer crack simulation coupling the phase field approach and cohesive zone model. *Compos Struct*. 2017;182:636-651.
27. Borden MJ, Hughes TJR, Landis CM, Anvari A, Lee IJ. A phase-field formulation for fracture in ductile materials: finite deformation balance law derivation, plastic degradation, and stress triaxiality effects. *Comput Methods Appl Mech Eng*. 2016;312:130-166.
28. Gültekin O, Dal H, Holzapfel GA. A phase-field approach to model fracture of arterial walls: theory and finite element analysis. *Comput Methods Appl Mech Eng*. 2016;312:542-566.
29. Fathi F, Ardakani SH, Dehaghani PF, Mohammadi S. A finite strain integral-type anisotropic damage model for fiber-reinforced materials: application in soft biological tissues. *Comput Methods Appl Mech Eng*. 2017;322:262-295.
30. Waffenschmidt T, Polindara C, Menzel A, Blanco S. A gradient-enhanced large-deformation continuum damage model for fibre-reinforced materials. *Comp Methods Appl Mech Eng*. 2013;268:801-842.
31. Brepols T, Wulfinghoff S, Reese S. Gradient-extended two-surface damage-plasticity: micromorphic formulation and numerical aspects. *Int J Plast*. 2017;97:64-106.
32. Junker P, Schwarz S, Jantos DR, Hackl K. A fast and robust numerical treatment of a gradient-enhanced model for brittle damage. *Int J Multisc Comput Eng*. 2019;17(2):151-180.
33. Vogel A, Junker P. Adaptive and highly accurate numerical treatment for a gradient-enhanced brittle damage model. *Int J Numer Methods Eng*. 2020;121(14):3108-3131.
34. Jantos DR, Hackl K, Junker P. An accurate and fast regularization approach to thermodynamic topology optimization. *Int J Numer Methods Eng*. 2019;117(9):991-1017.
35. Junker P, Balzani D. A new variational approach for the thermodynamic topology optimization of hyperelastic structures. *Comput Mech*. 2020;1-26.
36. Junker P, Balzani D. An extended Hamilton principle as unifying theory for coupled problems and dissipative microstructure evolution. *Contin Mech Thermodyn*. 2021;1-26.
37. Lemaitre J. Coupled elasto-plasticity and damage constitutive equations. *Comput Methods Appl Mech Eng*. 1985;51(1-3):31-49.
38. Lemaitre J, Desmorat R. *Engineering Damage Mechanics: Ductile, Creep, Fatigue and Brittle Failures*. Springer-Verlag; 2005.
39. Hackl K, Fischer FD, Svoboda J. A study on the principle of maximum dissipation for coupled and non-coupled non-isothermal processes in materials. *Proc Math Phys Eng Sci*. 2011;467:1186-1196.
40. Hackl K, Fischer FD. On the relation between the principle of maximum dissipation and inelastic evolution given by dissipation potentials. *Proc Royal Soc A Math Phys Eng Sci*. 2008;464(2089):117-132.
41. Carstensen C, Hackl K, Mielke A. Non-convex potentials and microstructures in finite-strain plasticity. *Proc Royal Soc Lond Ser A Math Phys Eng Sci*. 2002;458(2018):299-317.
42. Wriggers P. *Nonlinear Finite Element Methods*. Springer Science & Business Media; 2008.
43. Miehe C, Hofacker M, Welschinger F. A phase field model for rate-independent crack propagation: robust algorithmic implementation based on operator splits. *Comput Methods Appl Mech Eng*. 2010;199(45-48):2765-2778.
44. FEAP. A finite element analysis program. <http://projects.ce.berkeley.edu/feap/>

How to cite this article: Junker P, Riesselmann J, Balzani D. Efficient and robust numerical treatment of a gradient-enhanced damage model at large deformations. *Int J Numer Methods Eng*. 2022;123(3):774-793. doi: 10.1002/nme.6876